Mechanism and Machine Theory 195 (2024) 105605

Contents lists available at ScienceDirect

Mechanism and Machine Theory

journal homepage: www.elsevier.com/locate/mechmt

Research paper

Shape optimization of buckling-based deployable stiff structures

Hoo Min Lee [a,b], Gil Ho Yoon [a], Jonas Engqvist [b], Matti Ristinmaa [b], Mathias Wallin [b,*]

[a] Department of Mechanical Engineering, Hanyang University, Seoul 04763, South Korea
[b] Division of Solid Mechanics, Lund University, P.O. Box 118, SE-221 00 Lund, Sweden

ARTICLE INFO

Keywords:
Deployable structure
Buckling-induced deployment
Shape optimization
Tangent stiffness

ABSTRACT

This study considers deployable structures and presents a novel optimization method that aims to improve the stiffness at the fully deployed state. The considered structures consist of curved beams that deploy through buckling when rotated. The optimization aims to maximize the structural tangent stiffness by modifying the shape of the beam elements. To accurately predict the deformation, Finite Element Method (FEM) simulations were conducted. A design with an increase of up to 19.6% in structural tangent stiffness was achieved, while conserving the structural volume. The approach is validated by manufacturing the deployable structures using laser cutting and performing compression tests. Experimental results show consistency within a 5% range with the optimization results. These findings support the implementation of the optimization scheme for achieving optimum structural designs of deployable structures.

1. Introduction

Deployable structures have the ability to transform from compact configurations to expanded states [1] which make them popular in various engineering fields as solutions for efficient space utilization [2]. Studies have been conducted to utilize deployable structures for human lunar base [3], in-space assembled modular space telescope [4], space antennas [5], parabolic solid reflector [6], solar powered arrays [7,8], solar sails [9], and sun shields [10]. Deployable structures have also been recognized in the medical fields, such as deployable stents for human blood vessels [11,12], deployable meta-implants [13], and origami-inspired forceps in medical catheters [14]. In civil engineering, deployable structures realized origami-based shelters [15–17] and deployable bridges [18–20] to meet the needs of quick construction and convenient transportation. Deployable structures have also been applied to multi-functional robots for realization of self-folded origami exoskeletons [21], deformable wheels [22], and reconfigurable modular bodies [23].

Studies have also been done on the mechanisms of deployable structures, where investigation on multi-furcation behaviors [24–26] and stable state at each behavior [27] have been done numerically. Recent study in manufacturing smart furniture has demonstrated the potential of inducing deployment along a desired furcation path by tuning the characteristics of the buckling mode, showing the potential of deployable structures [28]. Our study aims to push this research further by maximizing the structural tangent stiffness. Since deployable structures have varying stiffness at different deployment stages [29], it is important to target the appropriate deployment phases. Following studies have considered the tangent stiffness to analyze structural mobility when subjected to external loads [30] and tune natural frequencies of deployable antenna structures [31]. Maximizing the tangent structural stiffness for nonlinear cases has been conducted in [32]. Thus, tangent stiffness maximization at the fully deployed state is considered in the study.

* Corresponding author.
E-mail address: mathias.wallin@solid.lth.se (M. Wallin).

https://doi.org/10.1016/j.mechmachtheory.2024.105605
Received 18 January 2024; Accepted 1 February 2024
Available online 8 February 2024

In the present study, structures composed of curved beams that deploy through buckling when subjected to rotational input are considered. The beam shape is parameterized using trigonometric functions and the objective is to design stiff structures when deployed. Since the deployed structure has passed a critical point and is subject to large deformation, the frequently used end-compliance cannot be used. Instead the objective is to maximize the tangent stiffness in the fully deployed state under a volume constraint. The structural problem is solved using FEM with shell elements in ABAQUS, whereas the optimization is solved using gradient-based optimization in MATLAB. A linear buckling analysis is used to identify the buckling modes that trigger the structural deployment. The nonlinear analysis that models the post-buckling deployment is solved using the Riks method. The design updates in gradient-based optimization requires sensitivity analysis. Since a commercial FEM software is used, the sensitivity analysis makes use of a perturbation technique to calculate the derivatives. As the number of design variables is limited this approach poses no challenges. The optimization was performed for an increasing number of design variables. The optimal designs were manufactured using laser cutting and compression experiments were conducted using an in-house test setup to validate the optimization results. The experimental verification shows that the proposed optimization is able to significantly improve the stiffness without increasing the volume of the structure.

The remainder of this paper is organized as follows. Section 2 provides background to the deployment mechanism and presents the numerical analysis method. Section 3 details the optimization formulation and presents the optimization results. Section 4 describes the experimental methods and validation of the optimization scheme. Conclusions and future topics are discussed in Section 5.

2. Deployment mechanism

2.1. Initial design

The deployable structure consists of six curved elastic beams with constant in-plane curvatures as shown in Fig. 1(a). To be compatible with the fabrication and experimental setup, centimeter-scale is considered. Each beam has an initial opening angle θ of 90° and an inner radius of 60 mm. The beams have a rectangular cross-section with width of 5.0 mm and a thickness of 1.0 mm. The ends of the beams move along a circular guide path with a radius of 75 mm with the center offset 25 mm. The schematic of a single circular beam is presented in Fig. 1(b). To deploy the beam, one end is fixed in its initial position, while the other end is displaced along the circular guide path. This displacement is applied in a direction that separates the two ends of the beams, such that the opening angle increases from 90° to θ>90°. When the opening angle reaches a critical value 90°+$\Delta\theta_{cr}$, the elastic beams start to buckle such that a 3D configuration is generated.

The structure is realized by overlapping two parts that are manufactured using a Legend 36EXT Epilog laser cutting machine from polyethylene terephthalate glycol (PETG) plastic sheets with a thickness of 1.0 mm. The parts that serve as the bottom layers (red) are flipped and rotated by 90°, before merging with the parts that serve as the top layers (light blue). The two layers overlap 5 mm at the ends of the half-length curved beams. Each pair of half-length curved beams are bonded at this overlapping region using Loctite 495 super glue to form six full-length beams. The illustration of this assembly process is shown in Fig. 1(c). It can be observed that one end of each beam is connected to the top layer and the other end to the bottom layer. This allows the structure to deploy when the bottom layer is rotated $\Delta\theta$ relative to the top layer. The transformation from the initial 2D configuration to a deployed 3D geometry are shown in Fig. 1(d), as a result of the rotational input $\Delta\theta$ by 90° counter-clockwise to the top layer. The rotation generated an average out-of-plane displacement of 65.8 mm. The structure can be realized as a deployable table, compact for transportation and storage, requiring simple assembly, and easily expanded by applying rotational input. The experimental snapshot is shown in Fig. 1(e), where the deployed beams act as the table legs, see also [28].

2.2. Numerical analysis

To perform shape optimization and obtain the global stiffness matrix of the deployable structure, the mechanical boundary value problem is solved using the FEM. ABAQUS 2021/Standard was used to solve the linearized buckling problem and analyze the post-buckling behavior of a single elastic beam. The linearized buckling analysis was performed to predict $\Delta\theta_{cr}$ and the first buckling mode. The structure was discretized using S4R four-node shell elements, and the material was modeled with a Young's modulus of 2.0 GPa and a Poisson's ratio of 0.4. One end of the beam was clamped while the other end was subject to a prescribed rotational displacement using a kinematic coupling constraint to the reference center point, P. To validate the linear buckling analysis, simulations with varying numbers of elements were conducted. The number of elements in the width direction was fixed to three. The results, as shown in Fig. 2(a), demonstrate that $\Delta\theta_{cr}$ converges for 200 elements. Based on these findings, the beam structure was modeled with 288 elements and 388 nodes in the subsequent post-buckling analysis and optimization procedures.

After the initial buckling analysis, a nonlinear static analysis was conducted to investigate post-buckling behavior. The first buckling mode was injected in the mesh to cause a small imperfection which triggered the first buckling mode. The infinity norm of the displacement imperfection is 1.0 mm. A 90° rotational input was applied to the unclamped end of the beam to investigate the deployment behavior. Snapshots of the deformation are presented in Fig. 2(b). The application of rotational input $\Delta\theta$ by 90° generated an out-of-plane displacement of 65.2 mm, which is very close to the actual average out-of-plane displacement of 65.8 mm, demonstrating the accuracy of the FEM analyses. The global stiffness matrix of the structure was obtained following the completion of the nonlinear static analysis, during which no further finite displacements occurred.

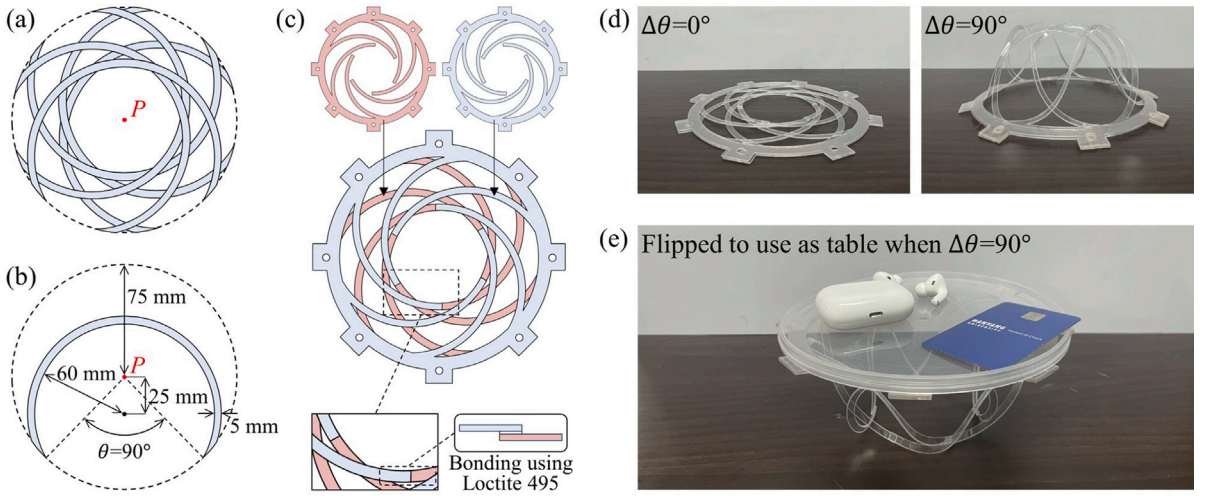

Fig. 1. Buckling-based deployable structure: (a) Schematics of deployable structure, (b) schematics of a single curved beam, (c) illustration of the assembly process, (d) snapshots of structure at rotational inputs of 0° and 90°, and (e) example application of structure being used as a table.

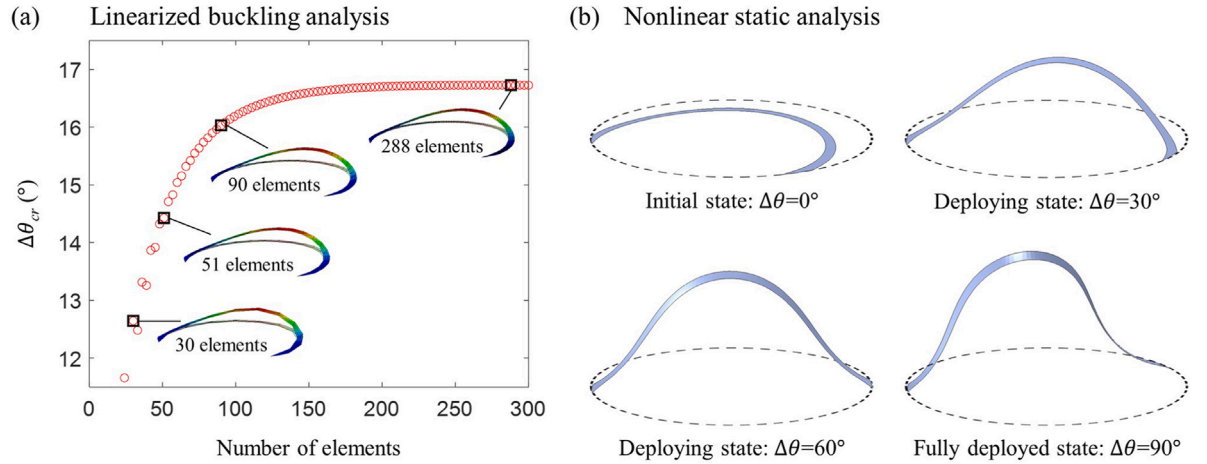

Fig. 2. (a) Changes in critical rotation angles with different number of finite elements in linearized buckling analysis and (b) changes in deployment geometry with increasing opening angles in nonlinear static analysis.

3. Shape optimization

3.1. Optimization formulation

The beam element shape is parameterized using trigonometric functions so that the parametrization is guaranteed to be smooth. The inner and outer beam edges were parameterized using

$$R_i = (0.060 + \sum_{i=1}^{n} a_i \sin\{(i-1)\varphi\})\ \mathrm{m}$$
$$R_o = (0.065 + \sum_{i=1}^{n} b_i \sin\{(i-1)\varphi\})\ \mathrm{m} \quad (1)$$

where R_i and R_o denote the undeformed radii of the inner and outer edges of the curved beam element along the polar angle φ. The $i = 1, \ldots, n$ design variables for inner and outer edges are denoted a_i and b_i, respectively. Based on the shape parametrization, the optimization problem was stated as finding the design $\mathbf{z}=[a_1, a_2, \ldots, a_n, b_1, b_2, \ldots, b_n]$ that solves

$$\begin{aligned} &\text{Minimize } g_0(\mathbf{z}) \\ &\text{Subject to } g_1(\mathbf{z}) < 0,\ |z_i| \le \Delta \end{aligned} \quad (2)$$

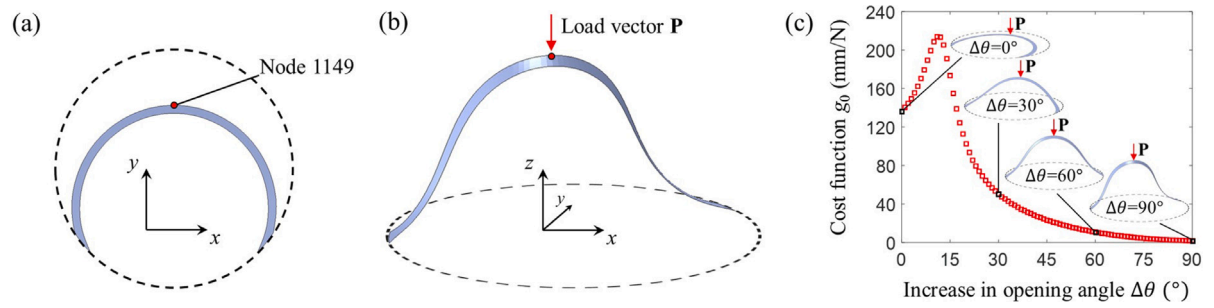

Fig. 3. (a) Position of node 1149, (b) definition of the load pattern vector **P**, and (c) relation between increase in opening angle $\Delta\theta$ and cost function g_0.

where g_0 and g_1 are the cost function to be minimized and the constraint function, respectively. The elements comprising a_i and b_i in the design variable vector $\mathbf{z}$ are denoted as z_i. In the numerical examples Δ=1 mm.

To define the tangent stiffness quantified in g_0, we consider the residual equilibrium equation,

$$\mathbf{R}(\mathbf{a}(\lambda), \lambda) = \mathbf{F}_{int} - \mathbf{F}_{ext} = \mathbf{F}_{int} - \lambda\mathbf{P} = \mathbf{0} \tag{3}$$

where $\mathbf{a}$, λ, $\mathbf{F}_{int}$, $\mathbf{F}_{ext}$, and $\mathbf{P}$ are the nodal displacement vector, load intensity, internal force vector, external force vector, and unit constant load pattern vector, respectively. The load pattern vector $\mathbf{P}$ is defined, as depicted in Figs. 3(a) and (b), on a single node located at the center of the outer edge in the deployment direction. Linearizing Eq. (3) with respect to λ yields

$$\frac{\partial \mathbf{R}}{\partial \mathbf{a}}\mathbf{a}' + \frac{\partial \mathbf{R}}{\partial \lambda} = \mathbf{K}\mathbf{a}' - \mathbf{P} = \mathbf{0} \tag{4}$$

where $\mathbf{a}'=\frac{\partial \mathbf{a}}{\partial \lambda}$ and $\mathbf{K}=\frac{\partial \mathbf{R}}{\partial \mathbf{a}}$ is the tangent stiffness matrix. Thus maximizing the tangent stiffness at the load intensity λ in the direction of $\mathbf{P}$ is equivalent to minimizing $\mathbf{P}^{\mathrm{T}}\mathbf{a}'$ [32]. Hence, the cost function which is to be minimized is defined as

$$g_0 = \mathbf{P}^{\mathrm{T}}\mathbf{a}' = \mathbf{P}^{\mathrm{T}}\mathbf{K}^{-1}\mathbf{P} \tag{5}$$

The structural volume is constrained in the optimization, i.e.

$$g_1 = \frac{V_{opt}(\mathbf{z})}{V_{ini}} - 1 \leq 0 \tag{6}$$

where V_{opt} and V_{ini} are the volumes of optimized structure and initial structure, respectively. Note that $V_{opt}(\mathbf{0})=V_{ini}$. The sensitivity of the cost function is

$$\frac{\partial g_0}{\partial \mathbf{z}} = \mathbf{P}^{\mathrm{T}}\frac{\partial \mathbf{K}^{-1}}{\partial \mathbf{z}}\mathbf{P} \tag{7}$$

where the derivative $\frac{\partial \mathbf{K}^{-1}}{\partial \mathbf{z}}$ was computed numerically by perturbation.

Before optimizing the structure, we analyze the tangent stiffness for increase opening angles. Tangent stiffness increases until $\Delta\theta$=11° is reached, after which it continues decreasing and becomes g_0=1.83 mm/N when $\Delta\theta$=90°, as shown in Fig. 3(c). The optimization aims to minimize g_0 at $\Delta\theta$=90°, hence maximizing the tangent stiffness of the deployable structure at its fully deployed state.

3.2. Optimization results

We start by performing optimizations for different number of design variables to explore the relationship between design space size and the optimized tangent stiffness, g_0. The $2n$ design variables correspond to n on the inner and n on the outer edges. The optimization process was performed using the gradient-based fmincon MATLAB built-in function. A case with 4 design variables was analyzed using fmincon and the MATLAB genetic algorithm (GA) optimizer to compare computational time and results. Optimization was carried out with the design variable perturbation 0.005 mm. The g_0 value was reduced to 1.66 mm/N for both methods. However, notable differences were observed in computational time, with the gradient-based optimizer requiring 68 function calls and GA requiring 868 function calls to converge to the optimized design. Considering its efficiency, the gradient-based optimizer was selected for the subsequent optimizations. The sensitivity results for the design variables are presented in Table 1 for reference.

For the representative cases using 4 (design 1), 10 (design 2), and 30 (design 3) design variables, the optimization reduced the g_0 value to 1.66 mm/N, 1.50 mm/N, and 1.47 mm/N, respectively. The results are presented in Fig. 4(a), where g_0 decreases monotonically as the number of design variables is increased. The 30 design variable case showed the greatest stiffness increase, with a g_0 decrease of 19.6% compared to the uniform width design. It is noteworthy that only minor improvements are obtained if more than 20 design variables are included. To evaluate design symmetry, two additional optimizations were conducted by exclusively incorporating symmetric modes. These cases employed 10 (design 4) and 20 (design 5) design variables. Their resulting g_0 values are presented in Fig. 4(a), where it can be seen that the symmetric designs exhibit minor reduction compared to the asymmetric

Table 1
Sensitivity analysis of design variables with perturbation values of 0.005 mm.

Design variable	a_1	a_2	a_3	a_4	a_5	a_6	a_7	a_8	a_9	a_{10}
Sensitivity (mm/N)	−0.14390	0.00305	−0.00104	0.00262	−0.14885	0.00106	−0.00042	0.00091	−0.00017	−0.00058
Design variable	a_{11}	a_{12}	a_{13}	a_{14}	a_{15}	b_1	b_2	b_3	b_4	b_5
Sensitivity (mm/N)	−0.00008	−0.00003	0.00000	0.00005	−0.14909	−0.00485	−0.15130	−0.14856	−0.00309	−0.00030
Design variable	b_6	b_7	b_8	b_9	b_{10}	b_{11}	b_{12}	b_{13}	b_{14}	b_{15}
Sensitivity (mm/N)	−0.14992	−0.14895	−0.00139	−0.14913	0.00110	0.00003	−0.00049	0.00000	0.00042	−0.00013

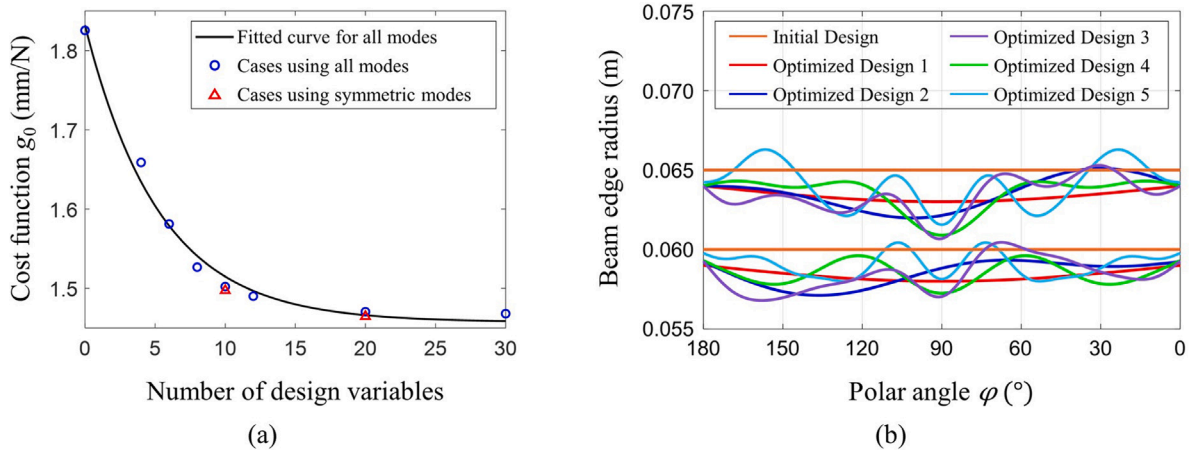

Fig. 4. (a) Relationship between number of design variables and tangent stiffness values ($g_0 = 0.3749e^{-0.1874n} + 1.4572$) and (b) changes in edge designs for different cases of shape optimization.

designs for cases using 10 and 20 design variables, respectively. The changes in edge designs for different cases are shown in Fig. 4(b). Initially, the radii values of the inner and outer edges were 0.060 m and 0.065 m, respectively. Fig. 5(a) illustrates the geometry changes resulting from optimization. A comparison between the initial and optimized design 3 clearly shows the geometric modification.

4. Experimental validation

To experimentally validate the optimized designs, three designs were manufactured and tested: symmetric design 1 and the geometrically challenging asymmetric designs 2 and 3. The structures were fabricated using the manufacturing process detailed in section 2.1. The two fabricated structures shown in Figs. 5(b) and (c) correspond to the initial design and optimized design 3. Both structures consist of six curved beams, with one end of each beam connected to the top layer and the other end connected to the bottom layer so that the structures deploy when the bottom layer is rotated relative to the top layer.

The fabricated structures' tangent stiffness were tested using the in-house developed compression test set-up shown in Fig. 6. An EZ-S Shimadzu Tester was used to apply load using an attached metallic plate, which moved vertically downwards at a constant speed of 5 mm/min. The load–displacement response was monitored using a Labview based control software. To ensure constrained boundary conditions for the circular edge of the structure, a polycarbonate ring structure was manufactured and placed over the deployable structure, and both structures were fixed to the bottom plate of the tester using eight bolts. Since the optimization was carried out for a single beam structure, the compression test was conducted on single beams for experimental validation. Bonding of half-length curved beams was done for each pair at a time before each experimental trial to ensure that only one of the beam structures deploys into a 3D geometry while the rest remain flat in their 2D configurations. Six trials were conducted for each design.

The compression test results are presented in Fig. 7. Each design was evaluated by averaging the results of six trials. The load–displacement graph shows that the results align with the finite element simulation and that increasing number of design variables leads to better performing structures, i.e. a higher tangent stiffness. The design 3 which used 30 design variables showed the greatest stiffness. To validate the FEM analyses, the tangent response at the deployed state of each design shown in Fig. 7(b) was evaluated. The incremental displacement for a small load perturbation of 0.1 N were experimentally determined. The initial design was displaced 0.178 mm due to the load perturbation. The optimized designs 1, 2, and 3 were displaced 0.162 mm, 0.154 mm, and 0.140 mm, respectively. Thus, the resulting experimental tangent stiffness is 1.78 mm/N (non-optimized design), 1.62 mm/N (design 1), 1.54 mm/N (design 2), and 1.40 mm/N (design 3). When compared with the FEM-based results presented in Section 3, the differences were found to be 2.3%, 2.5%, 2.8%, and 4.9%, respectively. The experimental results showed consistency with the FEM-based results within a 5% range for all four designs. These findings support the proposed shape optimization method as a means of maximizing tangent stiffness of deployable structures.

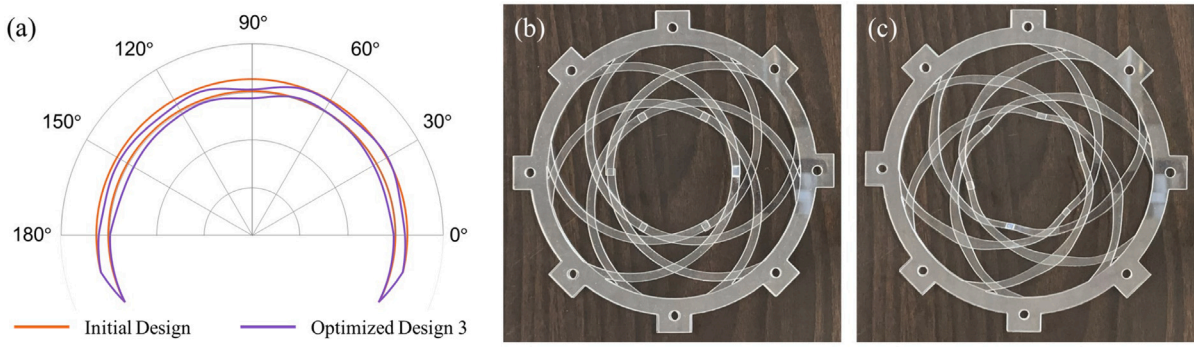

Fig. 5. (a) Comparison between the curved beam geometries of initial design and optimized design 3, (b) assembled structure with initial design before optimization, and (c) assembled structure with optimized design 3.

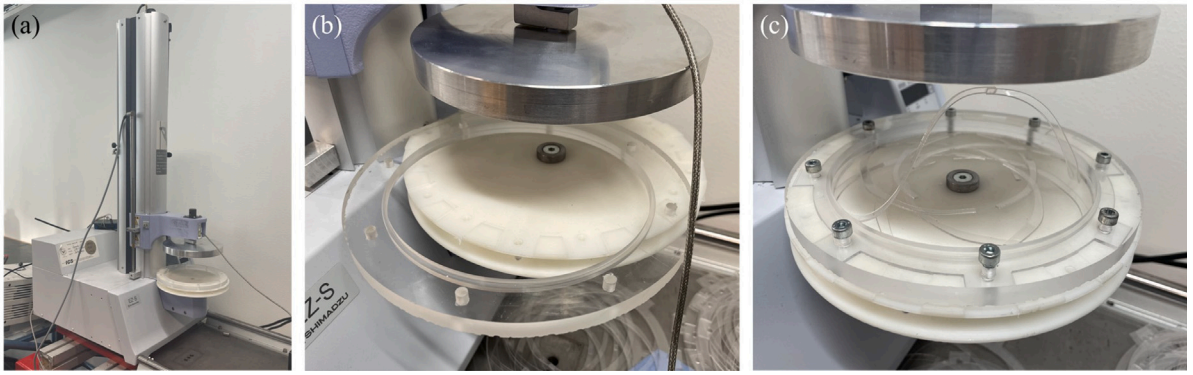

Fig. 6. Compression test equipment setup: (a) EZ-S Shimadzu Tester, (b) polycarbonate ring to realize constrained edges and (c) compression test conducted on a single beam.

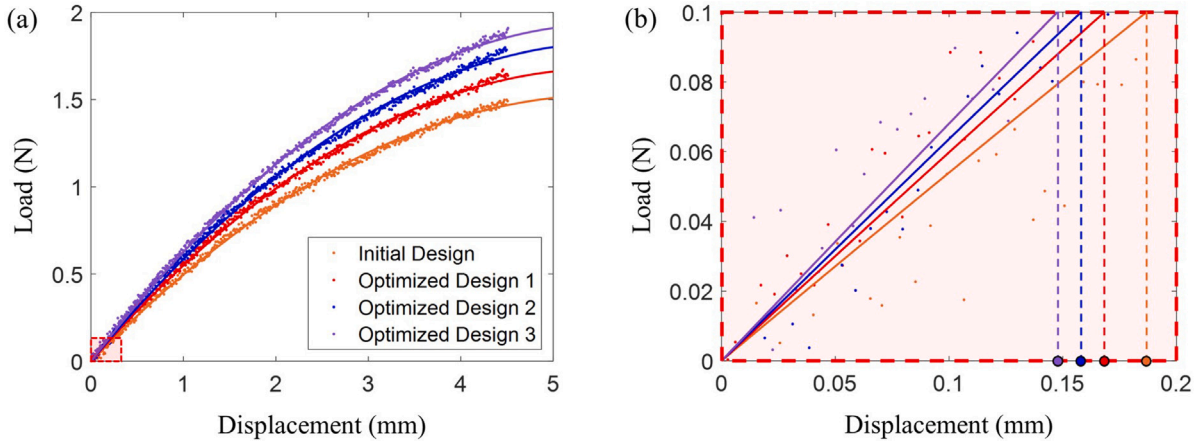

Fig. 7. Results of compression test for deployable structures with different designs: (a) nonlinear load–displacement relations and (b) linear load–displacement relations at the deployed state when applied with small loads.

5. Conclusions

This study presents an optimization framework to increase the stiffness of deployable structures when fully deployed. Structures consisting of curved beams were shape optimized. Trigonometric functions were used to parameterize the structures. The tangent stiffness was maximized under a volume constraint. FEM structural analysis, sensitivity analysis, and gradient based design updates were performed to update the designs. The optimized designs were up to 19.6% stiffer than the initial design. Structures were

manufactured using laser cutting and compression tests were conducted to validate the optimization results. The experimental results were compared to FEM simulation which deviated less than 5% for all tested structures. This study supports that the proposed shape optimization method is able to significantly improve the structural stiffness of deployable structures.

CRediT authorship contribution statement

Hoo Min Lee: Data curation, Formal analysis, Investigation, Visualization, Writing – original draft. **Gil Ho Yoon:** Conceptualization, Methodology, Supervision. **Jonas Engqvist:** Investigation, Writing – review & editing. **Matti Ristinmaa:** Supervision, Validation, Writing – review & editing. **Mathias Wallin:** Conceptualization, Investigation, Methodology, Project administration, Supervision, Validation, Writing – review & editing.

Declaration of competing interest

The authors declare that they have no known competing financial interests or personal relationships that could have appeared to influence the work reported in this paper.

Data availability

Data will be made available on request.

Acknowledgments

This research was supported by the MOTIE (Ministry of Trade, Industry, and Energy) in Korea, under the Fostering Global Talents for Innovative Growth Program (P0017307) supervised by the Korea Institute for Advancement of Technology (KIAT) and STINT (MG2020-8839).

References

[1] N. De Temmerman, L. Alegria Mira, A. Vergauwen, H. Hendrickx, W. De Wilde, Transformable structures in architectural engineering, High Perform. Struct. Mater. 6 (124) (2012) 457–468.
[2] T.-H. Kim, J.-E. Suh, J.-H. Han, Deployable truss structure with flat-form storability using scissor-like elements, Mech. Mach. Theory 159 (2021) 104252.
[3] P. Gruber, S. Häuplik, B. Imhof, K. Özdemir, R. Waclavicek, M.A. Perino, Deployable structures for a human lunar base, Acta Astronaut. 61 (1–6) (2007) 484–495.
[4] N. Lee, P. Backes, J. Burdick, S. Pellegrino, C. Fuller, K. Hogstrom, B. Kennedy, J. Kim, R. Mukherjee, C. Seubert, Y.-H. Wu, Architecture for in-space robotic assembly of a modular space telescope, J. Astron. Telescopes Instrum. Syst. 2 (4) (2016) 041207.
[5] Z. You, Deployable structure of curved profile for space antennas, J. Aerosp. Eng. 13 (4) (2000) 139–143.
[6] S. Nassehpour, A.S. Kwan, New concepts in large deployable parabolic solid reflectors, in: Proceedings of the AECEF Symposium, Vol. 6, Vilnius Gediminas Technical University, Department of Construction Economics & Property, 2008, p. 162.
[7] S.A. Zirbel, R.J. Lang, M.W. Thomson, D.A. Sigel, P.E. Walkemeyer, B.P. Trease, S.P. Magleby, L.L. Howell, Accommodating thickness in origami-based deployable arrays, J. Mech. Des. 135 (11) (2013).
[8] D.M. Murphy, M.I. Eskenazi, M.E. McEachen, J.W. Spink, UltraFlex and MegaFlex-development of highly scalable solar power, in: 2015 IEEE 42nd Photovoltaic Specialist Conference, PVSC, IEEE, 2015, pp. 1–8.
[9] L. Johnson, M. Whorton, A. Heaton, R. Pinson, G. Laue, C. Adams, NanoSail-D: A solar sail demonstration mission, Acta Astronaut. 68 (5–6) (2011) 571–575.
[10] L. Wilson, S. Pellegrino, R. Danner, Origami sunshield concepts for space telescopes, in: 54th AIAA/ASME/ASCE/AHS/ASC Structures, Structural Dynamics, and Materials Conference, 2013, p. 1594.
[11] S.H. Duda, J. Wiskirchen, G. Tepe, M. Bitzer, T.W. Kaulich, D. Stoeckel, C.D. Claussen, Physical properties of endovascular stents: an experimental comparison, J. Vascular Interventional Radiol. 11 (5) (2000) 645–654.
[12] K. Kuribayashi, K. Tsuchiya, Z. You, D. Tomus, M. Umemoto, T. Ito, M. Sasaki, Self-deployable origami stent grafts as a biomedical application of Ni-rich TiNi shape memory alloy foil, Mater. Sci. Eng. A 419 (1–2) (2006) 131–137.
[13] F. Bobbert, S. Janbaz, A. Zadpoor, Towards deployable meta-implants, J. Mater. Chem. B 6 (21) (2018) 3449–3455.
[14] B.J. Edmondson, L.A. Bowen, C.L. Grames, S.P. Magleby, L.L. Howell, T.C. Bateman, Oriceps: Origami-inspired forceps, in: Smart Materials, Adaptive Structures and Intelligent Systems, Vol. 56031, American Society of Mechanical Engineers, 2013, V001T01A027.
[15] T.-U. Lee, J.M. Gattas, Geometric design and construction of structurally stabilized accordion shelters, J. Mech. Robot. 8 (3) (2016) 031009.
[16] I.a.N. De Temmerman, M. Mollaert, I.a.T. Van Mele, I.a.L. De Laet, Design and analysis of a foldable mobile shelter system, Int. J. Space Struct. 22 (3) (2007) 161–168.
[17] X. Liu, J.M. Gattas, Y. Chen, One-DOF superimposed rigid origami with multiple states, Sci. Rep. 6 (1) (2016) 36883.
[18] Y. Chikahiro, I. Ario, P. Pawlowski, C. Graczykowski, M. Nakazawa, J. Holnicki-Szulc, S. Ono, Dynamics of the scissors-type mobile bridge, Proc. Eng. 199 (2017) 2919–2924.
[19] L. Zhu, D. Zhang, F. Shao, Q. Xu, Q. Zhao, Structural evaluation of torsional rigidity of new FRP–aluminum space truss bridge with rigid transverse braces, KSCE J. Civ. Eng. 23 (2019) 3021–3029.
[20] A. Teixeira, M. Pfeil, R. Battista, Structural evaluation of a GFRP truss girder for a deployable bridge, Compos. Struct. 110 (2014) 29–38.
[21] S. Miyashita, S. Guitron, S. Li, D. Rus, Robotic metamorphosis by origami exoskeletons, Science Robotics 2 (10) (2017) eaao4369.
[22] D.-Y. Lee, J.-S. Kim, S.-R. Kim, J.-S. Koh, K.-J. Cho, The deformable wheel robot using magic-ball origami structure, in: International Design Engineering Technical Conferences and Computers and Information in Engineering Conference, Vol. 55942, American Society of Mechanical Engineers, 2013, V06BT07A040.
[23] H. Banerjee, N. Pusalkar, H. Ren, Single-motor controlled tendon-driven peristaltic soft origami robot, J. Mech. Robot. 10 (6) (2018).
[24] Y. Qin, J.S. Dai, G. Gogu, Multi-furcation in a derivative queer-square mechanism, Mech. Mach. Theory 81 (2014) 36–53.

[25] G. Wei, Y. Chen, J.S. Dai, Synthesis, mobility, and multifurcation of deployable polyhedral mechanisms with radially reciprocating motion, J. Mech. Des. 136 (9) (2014) 091003.
[26] Y. Chen, J. Feng, Q. Sun, Lower-order symmetric mechanism modes and bifurcation behavior of deployable bar structures with cyclic symmetry, Int. J. Solids Struct. 139 (2018) 1–14.
[27] Y. Chen, R. Xu, C. Lu, K. Liu, J. Feng, P. Sareh, Multi-stability of the hexagonal origami hypar based on group theory and symmetry breaking, Int. J. Mech. Sci. 247 (2023) 108196.
[28] S. Mhatre, E. Boatti, D. Melancon, A. Zareei, M. Dupont, M. Bechthold, K. Bertoldi, Deployable structures based on buckling of curved beams upon a rotational input, Adv. Funct. Mater. 31 (35) (2021) 2101144.
[29] W. Wang, H. Rodrigue, S.-H. Ahn, Deployable soft composite structures, Sci. Rep. 6 (1) (2016) 20869.
[30] Y. Chen, J. Feng, Mobility of symmetric deployable structures subjected to external loads, Mech. Mach. Theory 93 (2015) 98–111.
[31] R. Liu, H. Guo, R. Liu, H. Wang, D. Tang, X. Song, Shape accuracy optimization for cable-rib tension deployable antenna structure with tensioned cables, Acta Astronaut. 140 (2017) 66–77.
[32] M. Wallin, N. Ivarsson, D. Tortorelli, Stiffness optimization of non-linear elastic structures, Comput. Methods Appl. Mech. Engrg. 330 (2018) 292–307.